Observation of Quasi-Invariant Photocarrier Lifetimes in PbS Nanocrystal Assemblies Coupled to Resonant and Nonresonant Arrays of Optical Antennas

Puyuan He, Augustin Caillas, Guillaume Boulliard, Ismail Hamdi, Pascal Filloux, Marco Ravaro, Emmanuel Lhuillier, Aloyse Degiron

▶ To cite this version:

Puyuan He, Augustin Caillas, Guillaume Boulliard, Ismail Hamdi, Pascal Filloux, et al.. Observation of Quasi-Invariant Photocarrier Lifetimes in PbS Nanocrystal Assemblies Coupled to Resonant and Nonresonant Arrays of Optical Antennas. ACS photonics, 2024, 11 (2), pp.437-444. 10.1021/acsphotonics.3c01232 . hal-04546466

HAL Id: hal-04546466
https://hal.science/hal-04546466v1

Submitted on 16 Apr 2024

Observation of quasi-invariant photocarrier lifetimes in PbS nanocrystal assemblies coupled to resonant and non-resonant arrays of optical antennas

Puyuan He[1], *Augustin Caillas*[1], *Guillaume Boulliard*[1], *Ismail Hamdi*[1], *Pascal Filloux*[1], *Marco Ravaro*[1], *Emmanuel Lhuillier*[2], *Aloyse Degiron*[1,*]

[1]Université Paris Cité, CNRS, Laboratoire Matériaux et Phénomènes Quantiques, 75013 Paris, France

[2]Sorbonne Université, CNRS, Institut des NanoSciences de Paris, INSP, F-75005 Paris, France

*aloyse.degiron@u-paris.fr

ABSTRACT: We examine, in the time domain, the influence of Au antenna arrays (i.e. metasurfaces) on thin films of near-infrared PbS nanocrystals that mutually interact via Förster Resonance Energy Transfer (FRET). While the geometry and optical properties of the arrays have a direct and sometimes spectacular impact on the transient photoluminescence spectra of the emitters, we experimentally show that the decay rate at any given wavelength is remarkably similar for all samples. This observation is in stark contrast with the textbook case of individual emitters weakly coupled to photonic structures. We show that FRET plays two key roles in these experiments—first, it is more efficient than other non-radiative energy transfers, including Joule dissipation in the optical antennas, for most wavelengths; second, it thermalizes the photocarriers of neighboring nanocrystals before their recombination, making them behave as an effective semiconducting material obeying a generalized form of Kirchhoff's law.

1. Introduction

Optical antennas have found many uses over the years beyond improving the pumping efficiency of quantum emitters, enhancing their brightness, and/or shaping their emission pattern and polarization[1]. When made of noble metals, optical antennas have been exploited for thermal engineering, taking advantage of surface plasmon resonances to induce controlled Joule heating at the nanoscale[2], or for generating hot electrons in Schottky barrier photodetectors[3] and solar cells[4]. Optical antennas have also been shown to enhance or suppress the Förster resonance energy transfer (FRET) rate between a donor and an acceptor[5,6] and to induce FRET in forbidden configurations, such as perpendicularly oriented donor-acceptor pairs[7].

Up to now, most studies on FRET influenced by optical antennas have focused on energy transfers between two specific pairs of donors and acceptors. There are, however, numerous systems in which emitters are both donors and acceptors. Such is the case, for example, of aggregates[8] and thin films[9–12] of colloidal nanocrystals (NCs) that offer interesting alternatives to epitaxial semiconductors for lighting, detection and energy harvesting applications. The NCs forming such media are always characterized by a certain dispersion in size, resulting in an inhomogeneous broadening of their absorption and emission bands. For certain NC assemblies, the inhomogeneous broadening can be quite substantial, on the order of ten percent or more of the central bandgap value, leading to significant changes in the ensemble emission spectrum, quantum efficiency and decay rates of the emitters due to mutual interactions via FRET and/or electronic coupling. In this article, we examine with time-resolved photoluminescence (PL) experiments the influence of arrays of optical antennas on ensembles of PbS NCs experiencing a substantial amount of FRET. While a rich diversity of spectral and intensity changes can be induced with different antenna geometries, we show that the decay rate of the PbS NCs at any given wavelength is remarkably similar in all cases. We identify two key roles played by FRET to explain this unexpected result and discuss the consequences of our findings for NC optoelectronics.

2. Results for thin films of PbS NCs coated on glass

The active medium considered in this study consists of 2 to 3 monolayers of closely packed colloidal PbS NCs capped with oleic acid ligands (see Supporting Information for details about the synthesis) and spun on a glass substrate. The steady-state PL spectrum of the NC layer, plotted in Figure 1a, exhibits an inhomogenously-broadened maximum centered on 1220 nm, which is typical for this type of material[13]. The asymmetry of the PL peak is also expected[10] due to FRET from the smallest NCs to the largest ones (i.e., those that emit at the longest wavelengths).

We study the temporal evolution of the PL by focusing the picosecond pulses of a laser diode (central wavelength 640 nm and repetition rate 1 MHz) onto the sample. The PL signal is collected with the same objective, directed to an interferometer that provides a spectral resolution to the measurements, and finally analyzed with a time-correlated single photon counting setup (see Figure S4 for a description of the apparatus).

The evolution of the PL spectrum over time is plotted as a color map in Figure 1b. The signal exhibits a broad maximum that shifts from 1200 nm to 1500 nm over a time span of approximately 200 ns, after which the spectrum shape and position do not change anymore. This evolution is better visualized in Figure 1c where we show the same map after renormalizing each transient spectrum by its maximum value and replotting the data over a longer time range. Figure 1d offers a different view of the same phenomenon, with a plot of the PL transients at five different wavelengths (1200 nm, 1250 nm, 1350 nm, 1450 nm and 1500 nm). To maximize the signal over noise ratio, these transients are not derived from the PL map of Figures 1b and 1c. Rather, they have been independently measured, without the interferometer, by successively filtering the PL signal with a series of bandpass filters with a half width at half maximum of 10 nm (see section 4.2 of the Supporting Information for more details).

The transient data plotted in Figure 1 are in good agreement with previous studies having documented FRET in thin layers of NCs[9–11]. In particular, the slow redshift of the emission as a function of time is consistent with a gradual energy transfer toward the largest NCs with the lowest bandgaps. Since FRET reduces the lifetime of the donors and raises that of the acceptors, we also expect to observe a gradual slow-down of the relaxation as the wavelength increases, which is precisely the behavior captured in Figure 1d.

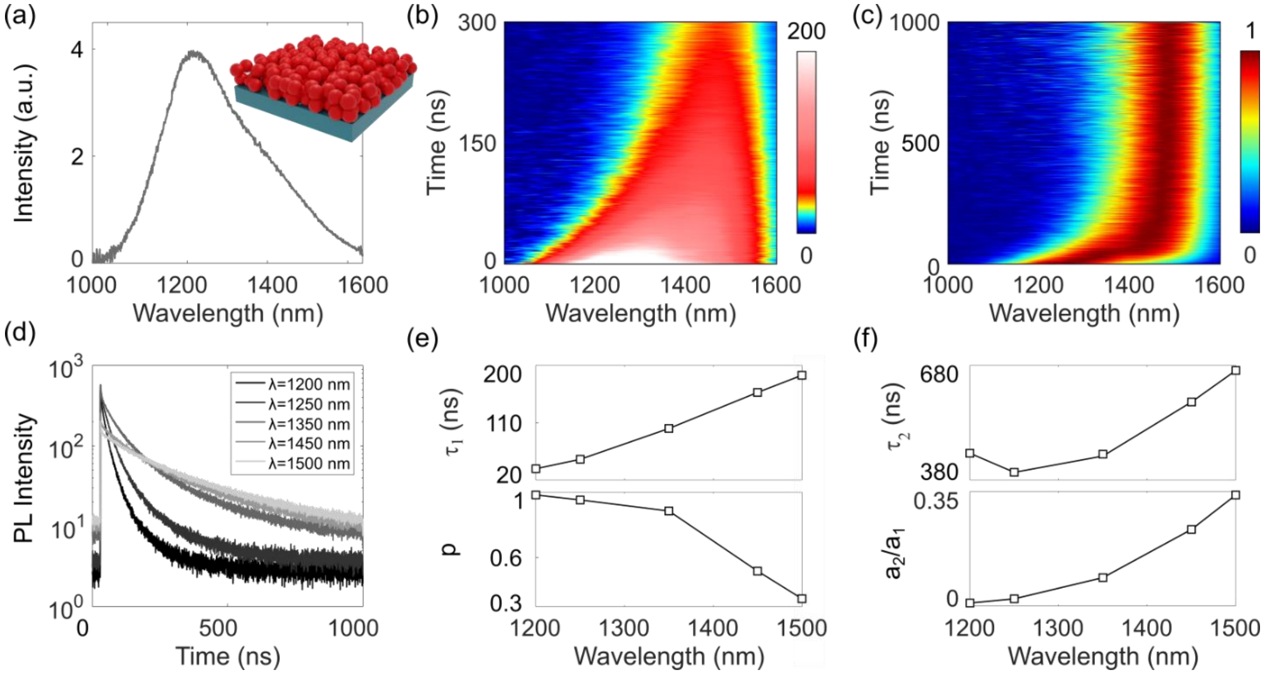

Figure 1. (a) PL spectrum of a thin film of PbS NCs on glass excited by a continuous HeNe laser at 633 nm. (b) Transient PL of the same sample as a function of time and wavelength λ. (c) Same data, plotted over an extended time range, after each transient spectrum has been normalized by its maximum value. (d) Transient PL decay at λ = 1200 nm (black), 1250 nm (darkest gray), 1350 nm (dark gray), 1450 nm (light gray) and λ = 1500 nm (lightest gray). (e) Characteristic time τ_1 and parameter p obtained by fitting the transients of panel (d) with Eq. (1). (f) Characteristic time τ_2 and ratio between a_2 and a_1, obtained by fitting the transients of panel (d) with Eq. (1).

In previous theoretical developments, the transient PL of emitters interacting by FRET was shown to follow a stretched exponential dependence of the form $I(t) \propto \exp(-t/\tau_1)\exp[-p(t/\tau_1)^{\beta}]$, with p a parameter determined by the concentration of acceptors and the Förster radius R_0 (estimated to be at least 8 to 9 nm in our case, see Supporting Information) and $\beta = 1/3$ for two-dimensional films or $\beta = 1/2$ for 3D nanocrystal solids[14,15].

To fit the transients data of Figure 1d with this model, we use $\beta = 1/3$ because we work with very thin films of two to three monolayers of PbS NCs. In addition, it was necessary to add two other exponentials to the fit—one, with characteristic time τ_0, to take into account the fast recombination of trions and/or multiexcitons, and another one, with characteristic time τ_2, to capture the slow decay from uncoupled NCs:

$$I(t) = a_0 \exp\left(-\frac{t}{\tau_0}\right) + a_1 \exp\left(-\frac{t}{\tau_1}\right) exp\left[-p\left(\frac{t}{\tau_1}\right)^{\frac{1}{3}}\right] + a_2 \exp\left(-\frac{t}{\tau_2}\right). \qquad (1)$$

The adjusted parameters are summarized in Table S1 and most of them are plotted in Figures 1e and 1f. The values are fully consistent with the role attributed to the three terms of Eq. (1). Table S1 indicates that $\tau_0 \sim 1$ ns and additional experiments summarized in Figure S7 show that the relative weight a_0 of this fast component increases non-linearly with the pump power, as expected for multiexcitons and/or trions. Figure 1e reveals that τ_1 experiences a 5.2-fold increase with the wavelength, from 37 ns at 1200 nm to 192 ns at 1500 nm, reflecting the gradual energy transfer from NCs emitting at short wavelengths to acceptors emitting at longer wavelengths. Simultaneously, the parameter p, which is proportional to the concentration of acceptors[15], tends to zero as the wavelength increases (Figure 1e). This behavior is physically consistent since the PL bandwidth does not extend beyond 1600 nm, implying that the density of NCs that can act as acceptors at wavelengths larger than 1500 nm becomes vanishingly small. As a corollary, the fraction of uncoupled NCs, represented by the last term of Eq. (1) with weight a_2 and characteristic time τ_2, must increase with λ. This behavior is well captured by our model, as can be appreciated with the evolution of the a_2/a_1 ratio plotted in Figure 1f. Importantly, a_2/a_1 is almost zero for the NC subpopulation emitting at the shortest wavelengths because all the other NCs have lower energy gaps and can therefore act as acceptors. Finally, Figure 1f shows that the characteristic time τ_2 associated with uncoupled NCs increases with the wavelength. While a similar dependence has been reported in the past for uncoupled PbS NCs[16], the increase of τ_2 is steeper in our case and it never reaches the microsecond lifetimes typical of PbS NCs in solution (see also next paragraph). This result indicates that the uncoupled NCs in our samples, while not being subjected to FRET, are still influenced by their environment via, e.g., photon reabsorption and interactions with the ligands.

To rule out other possible causes for these observations, we have verified that the transients could not be fitted with simpler functions, such as a sum of several exponentials. Moreover, we have established that the spectral shifts of Figure 1 do not depend on the input power (Figure S8), thus eliminating transient Joule heating and band-filling effects[17] as possible causes behind this behavior. Likewise, we have obtained similar PL maps with highly oxidized samples, as well as with PbS NC films in which the native oleic acid ligands have been replaced with much shorter 1,2-ethanedithiol (EDT) chains (Figures S9 and S10). Thus, the observations cannot be attributed to a mere superposition of excitonic recombination (without FRET) and trap state emission at two different central wavelengths, as the contribution of the latter strongly depends on the ligands and oxidation state of the NCs. We have also ensured that the features which we have attributed to FRET are not present when the PbS NCs are measured prior to their processing into thin solid films, i.e. when they are suspended in toluene and thus far apart from one another. Figure S11 shows that in this case, the PL kinetics has the behavior expected from an assembly of uncoupled emitters: the lifetime exceeds the µs, the decay is mono-exponential at all wavelengths and the PL peak does not shift to the red as the dynamics unfolds. Finally, we note that the FRET term used in Eq. (1) is a simplified expression that can only be used if the Förster radius is larger than the distance between neighboring NCs[15]. We have verified that the results presented in Figures 1e and 1f hold true when we perform the fits with the full expression.

3. Results for thin films of PbS NCs coated on Au metasurfaces

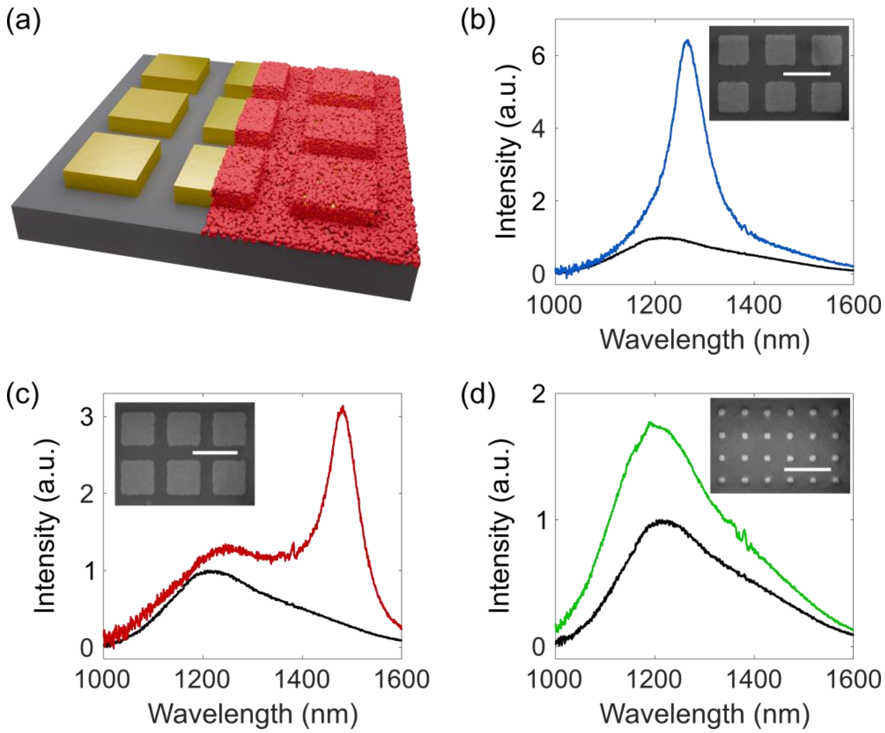

Figure 2. (a) Schematic of the samples with Au antenna arrays. For better visibility, the PbS NCs, represented as red spheres, are not drawn on the left side of the schematic. (b) PL spectrum of the PbS NCs coated on metasurface 1 (period of 550 nm and 330 nm × 330 nm × 25 nm Au patches). Also reproduced is the PL spectrum without antenna already plotted in the first panel of Figure 1 (black curve), as well as a scanning electron micrograph of the sample (inset). (c) Same plot for metasurface 2 (period of 600 nm and 400 nm × 400 nm × 25 nm Au patches). (d) Same plot for metasurface 3 (period of 300 nm and 80 nm × 80 nm × 25 nm Au patches). The scale bars of the insets represent 600 nm.

We now repeat the experiments with PbS NCs coated onto periodic arrays of square Au antennas (Figure 2a). As discussed in detail in section 3 of the Supporting Information, they have been designed to produce spectrally sharp analogues of electromagnetically induced absorption (EIA) resonances, resulting from the simultaneous excitation of dipolar surface plasmons on the Au antennas and LC magnetic resonances between the nanoparticles[18]. Because EIA typically occurs with subwavelength periods, these arrays operate below the onset of the first diffraction orders and therefore qualify as optical metasurfaces. In the following, we will consider three geometries. Metasurface 1, with a period of 550 nm and patch dimensions 330 nm × 330 nm × 25 nm, sustains an EIA resonance at $\lambda_1 = 1265$ nm when coated with the PbS NCs, resulting in a strong enhancement of the steady-state PL at this wavelength (Figure 2b) as well as a dispersion relation typical of EIA (Figure S1). Metasurface 2, with a period of 600 nm and patch dimensions 400 nm × 400 nm × 25 nm, supports an EIA resonance that enhances the PL at $\lambda_2 = 1480$ nm (Figures 2c and S2). Metasurface 3, with much smaller dimensions (period of 300 nm and Au particles measuring 80 nm × 80 nm × 25 nm), is a control sample without any resonance in the wavelength range considered in this study (Figures 2d and S3).

The transient PL maps are very sensitive to the wavelength of the EIA resonance. Specifically, the first sample with an EIA resonance at $\lambda_1 = 1265$ nm results in transient spectra with two peaks after roughly 100 ns, one centered on λ_1 and the other centered on the wavelength previously observed without antennas (Figure 3a). Moreover, the normalized data of Figure 3b show that the relative weight of the peak at λ_1 gradually increases at long times. Conversely, the second sample with an EIA resonance at $\lambda_2 = 1480$ nm reduces the apparent PL redshift, as a single peak around this wavelength is present during the full duration of the decay (Figures 3d and 3e). As for the non-resonant control sample, the measurements are quite similar to the PL map of Figure 1 recorded for PbS NCs on a bare glass substrate, except that the PL intensity has almost tripled (compare the colorbars of Figures 1b and 3g).

We attribute the PL enhancement of the nonresonant sample to the increased reflectivity induced by the Au patterns at the bottom of the PbS NC layer, redirecting part of the PL that would have otherwise been emitted in the substrate towards the detection apparatus on the air side. In addition,

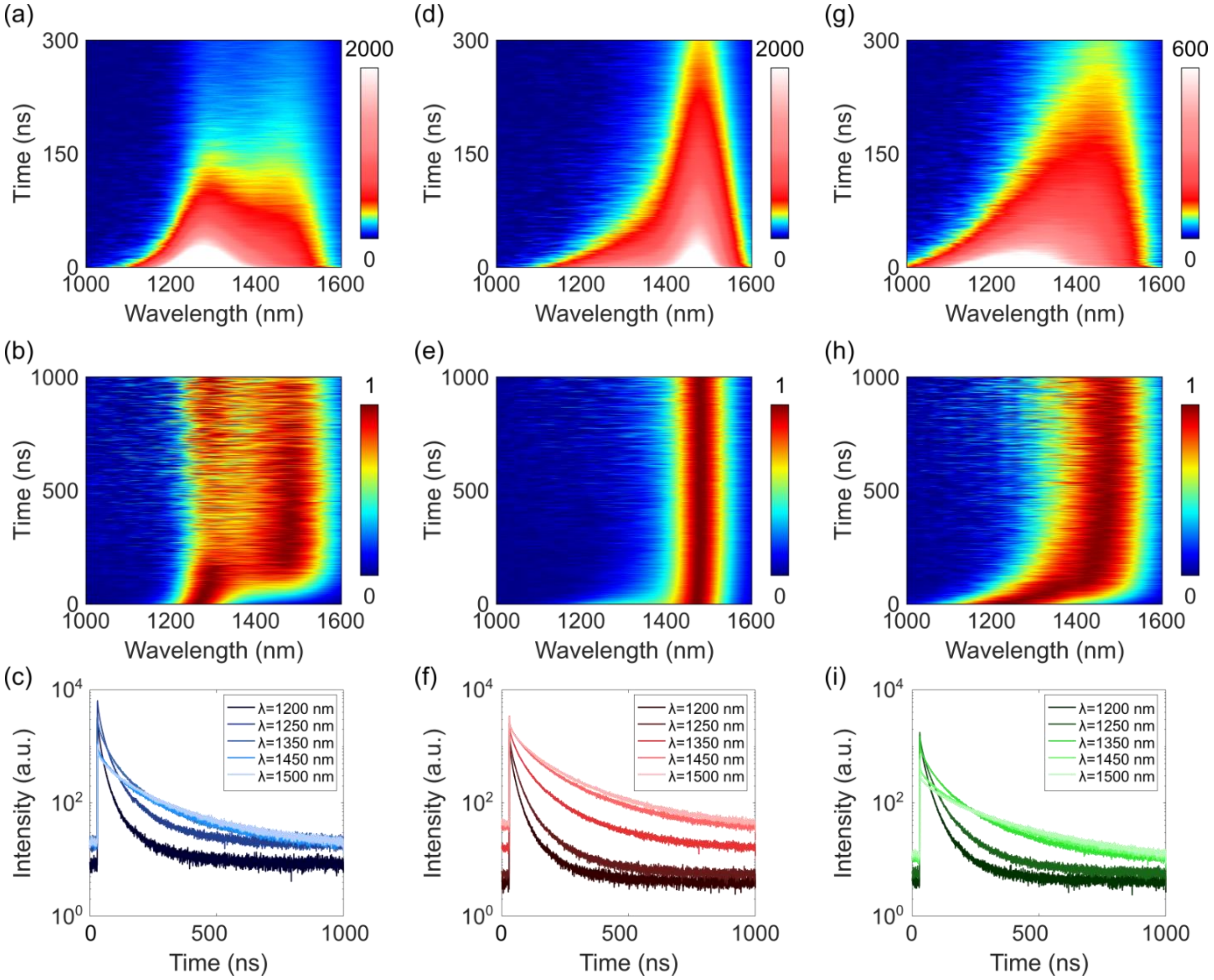

Figure 3. The top row shows the transient PL maps of the three samples with antennas described in the text and Figure 2. The excitation conditions and integration time are the same as those used in Figure 1 for characterizing the PbS NC film on glass. The middle row shows the same data after renormalizing each transient spectrum by its maximum value and extending the time range to 1 µs. The bottom row shows the transient PL traces at λ = 1200 nm, λ = 1250 nm, λ = 1350 nm, λ = 1450 nm, and λ = 1500 nm (from dark to light colors). (a,b,c) Sample resonant at λ_1 = 1265 nm (metasurface 1). (d,e,f) Sample resonant at λ_2 = 1480 nm (metasurface 2). (g,h,i) Non-resonant sample (metasurface 3).

the Au structures may also improve the pumping efficiency through efficient scattering of the excitation pulses. The PL enhancement achieved with the resonant structures of Figures 3a and 3d is significantly larger than that, the colorbars of these panels covering ten times the range used to display the data recorded without antenna in Figure 1b.

To understand this behavior, we examine, for each structure, the PL transients at the five wavelengths already considered with the PbS NC film deposited on glass (Figures 3c, 3f and 3i). Despite significant variations in the PL signal, the lifetime gradually increases with the wavelength in all three cases, and with approximately the same kinetics, regardless of the resonant or non-resonant nature of the antenna arrays.

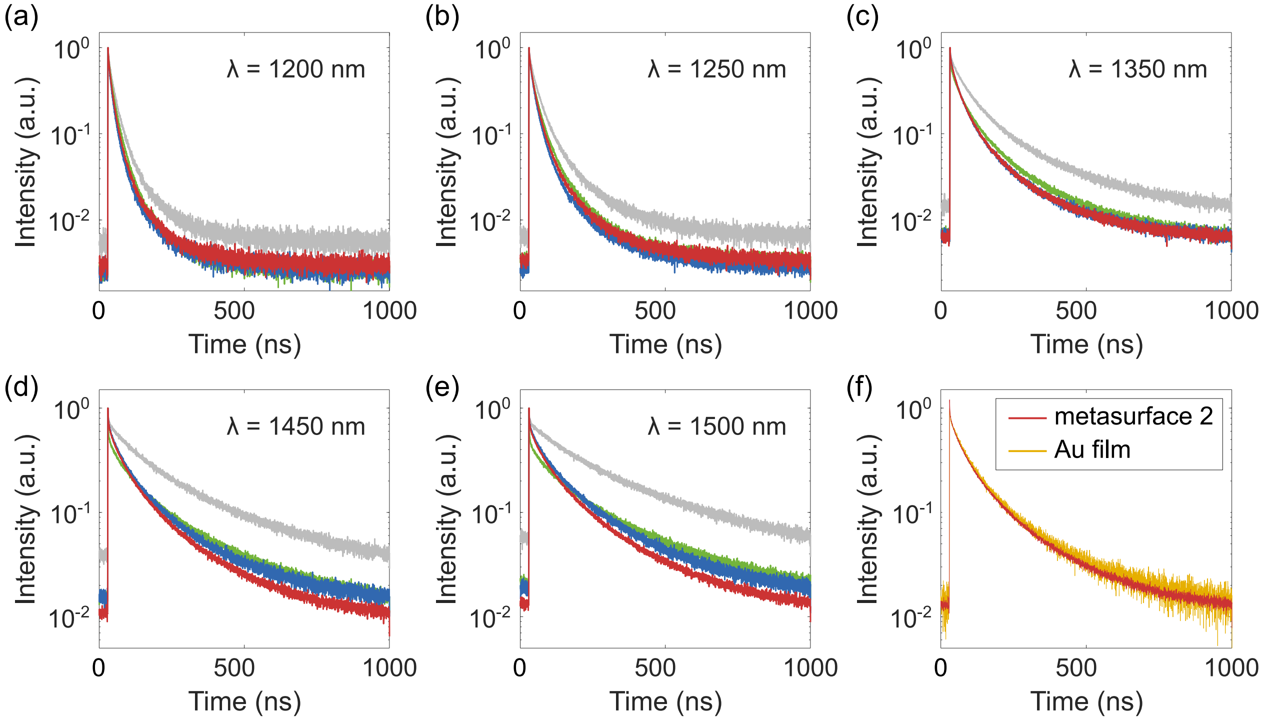

Figure 4. (a)-(e) Same material as Figure 1d and Figures 3c,f,i, but plotted differently. Each panel superimposes, at a given wavelength λ, the PL traces recorded for all the samples investigated in this study. All the traces have been normalized by their maximum value. Gray: PbS NCs on glass. Blue: sample resonant at λ_1 = 1265 nm (metasurface 1). Red: sample resonant at λ_2 = 1480 nm (metasurface 2). Green: Non-resonant antenna array (metasurface 3). Some curves are barely visible because they are almost perfectly superimposed with others. (f) Comparison between the decay trace of the structure resonant at λ_2 = 1480 nm (metasurface 2, in red) and the decay trace recorded with NCs covering a continuous Au film (in yellow). Data taken at λ = 1450 nm.

The similarities between the different traces can be further appreciated by normalizing all PL transients by their maximum value, as shown in Figure 4, where we have plotted, for each of the five wavelengths, the normalized PL transients of the three metasurfaces together with the one previously measured without Au antenna. Regardless of the wavelength, the PL decays faster when the PbS NCs are coupled with Au patterns, indicating, in good agreement with decades of literature on the subject, that optical antennas provide additional relaxation channels for the emitters[1]. More unexpected is the fact that the observed accelerations are rather modest and largely independent of the antenna geometry. For the smallest wavelengths, the normalized PL traces of the three samples patterned with Au are almost perfectly superimposed (see Figure 4a-4c, representing the decay traces at 1200 nm, 1250 nm and 1350 nm, respectively), which is all the more remarkable that only one of them has a strong EIA resonance in this spectral range (i.e. the structure with an EIA resonance at λ_1 = 1265 nm, cf. Figures 2b and 3a-b). In the two plots representing the decay traces at 1450 nm and 1500 nm, some differences start to appear between the structures. In particular, a steeper decay is observed for the sample having a resonance at λ_2 = 1480 nm.

To get quantitative insight, we note that the stretched exponential model previously used to depict FRET among the PbS NCs on glass also successfully describes energy transfers between emitters and optical antennas[15]. Thus, we can use Eq. (1) to fit the transients of Figures 3c, 3f and 3i by considering that a given NC can either exchange energy with one of its lower-bandgap neighbors via FRET or with the Au metasurface.

The results of the fits are given in Tables S2-S4. The characteristic times τ_0 and τ_2, which are, respectively, associated with the fast decay of trions/multiexcitons and the slow decay of the fraction of PbS NCs not subject to FRET, are only slightly altered by the presence of the antenna arrays. In contrast, the parameters τ_1 and p of the stretched exponential function associated with

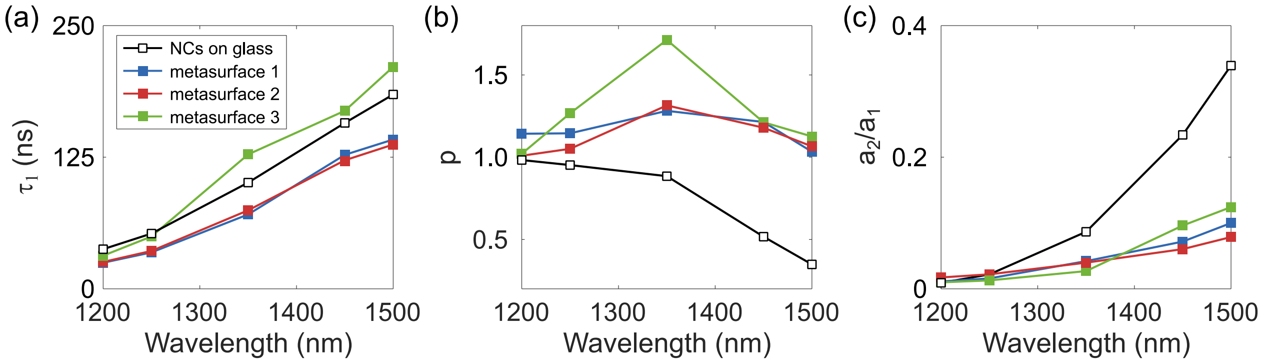

Figure 5. (a) Characteristic time τ_1 and (b) parameter *p* obtained by fitting all the transients of the study with Eq. (1). (c) Evolution of the ratio a_2/a_1 for the same cases.

energy transfers (FRET and coupling with the Au metasurfaces) exhibit new features plotted in Figure 5a and 5b, respectively, together with the results for the PbS NC film on glass already presented in Figure 1.

At small wavelengths, all the samples, including the PbS NCs on glass, display the same characteristic time τ_1. As λ becomes larger, τ_1 increases for all samples but significantly less so for the antenna arrays with EIA resonances at λ_1 = 1265 nm and λ_2 = 1480 nm (blue and red points). We attribute this behavior to the high fraction of Au in these two metasurfaces that reduces the lifetime of the PbS NCs by approximately the same amount due to higher Joule losses. To validate this hypothesis, we show in Figure 4(f) that the PL trace of the resonant sample at λ_2 = 1480 nm is almost indistinguishable from the decay obtained with PbS NCs spun on a non-resonant continuous Au film. A continuous Au film does not sustain any photonic radiating mode (but only non-radiative propagating surface plasmons); therefore, the energy transferred from the PbS NC film to the Au surface is eventually dissipated as Joule losses. In contrast, the non-resonant metasurface is characterized by a much smaller fraction of Au per unit cell, resulting in a characteristic time τ_1

almost identical to that of the PbS NC film on glass (compare green and open black symbols in Figure 5a).

The fact that the different samples are insensitive to the metal filling factor at smaller wavelengths (Figures 4a-c and Figure 5a) suggests that internal dissipation (via trap states) and energy exchange (FRET) within the NC film are more efficient than Joule losses in the metal. With this last element in mind, we can now analyze the evolution of the fitting parameter p. Figure 5b shows that the trajectory of this parameter is extremely similar for all three metasurfaces, including the non-resonant one, and becomes increasingly divergent from that of the PbS NCs on glass as λ increases. The values of p are not only higher for the samples patterned with Au, but they do not tend to zero at large wavelengths contrarily to the case of the PbS NCs on glass. This result can be explained by the fact that p is proportional to the concentration of acceptors[15], which, when we apply Eq. (1) to the resonant samples, does not only include the NCs with smaller bandgaps, but also the Au inclusions. Even though FRET does not occur at large wavelengths due to a lack of PbS NCs emitting further into the infrared (Figure 1), the parameter p cannot tend to zero for the three metasurfaces because the Au patches continue to act as acceptors via non-radiative quenching. As a corollary, a significant part of the PbS NCs that were left uncoupled without metasurface due to the lack of FRET at long wavelengths are now interacting with the Au inclusions, explaining why the transients become more sensitive to the metal filling factor and to the resulting non-radiative Joule losses that reduce the emitter's lifetime. This conclusion is further supported by the evolution of the ratio a_2/a_1, which characterizes the respective weights of uncoupled and coupled NCs. Figure 5c shows that this quantity is not only smaller than for the PbS NCs coated on glass, but also decreases with the Au filling factor.

4. Discussion

Taken together, these results indicate that the influence of optical antennas on the transient PL of an ensemble of inhomogenously-broadened emitters interacting by FRET is quite different from the textbook description valid for individual, non-interacting emitters[1]. In the latter case, the modifications of the PL by optical antennas are entirely explained by the local density of photonic states (LDOS) in their vicinity, which is typically higher than in their absence. This high LDOS provides additional radiative and non-radiative paths for excited emitters to relax to their ground states. The acceleration of the decay rate that ensues, i.e., the Purcell effect, critically depends on the optical properties of the antennas and can be accurately predicted with Fermi's golden rule[1,19,20]. The luminescence will be enhanced if the radiative relaxation channels outnumber the non-radiative ones and quenched in the opposite case. For metallic antennas, which are characterized by high material losses, the threshold between PL enhancement and quenching depends on the distance at which the emitters are placed. At vanishing distances, all the energy is essentially lost by Joule effects in the metal[1].

The present case differs from this textbook situation by two outstanding aspects. First, the PL is not quenched even though the emitters are placed in direct contact with the lossy Au patterns, a phenomenon that we have already reported in the steady-state regime[18,21–23], including for very lossy metals such as Pt in the near-infrared[22], and that we presently explain by the fact that energy transfer among the NCs is more efficient than energy dissipation in the metal over most of the emission band (see previous discussion around Figures 4 and 5). Second, the three antenna arrays presented in this study have essentially the same effect on the lifetime of the emitters, even though two of them have sharp resonances at very different wavelengths and the last one is non-resonant over the full emission band of the PbS NCs. Thus, the stark differences between the PL efficiencies and spectral features of the different samples (Figure 3) can only be explained by differences in the balance between radiative and non-radiative decay channels. In other words, the primary role of the antenna arrays in these experiments is not to change the emitter's lifetime, but rather to modulate spectrally the emissivity of the NC film—and, by reciprocity, its absorption cross-section at the wavelength of emission. One recognizes in this conclusion the main statement of the generalized Kirchhoff's law—a model initially developed to describe the thermal, photo- and electro-luminescence of bulk materials at thermal equilibrium[24] and later formally extended, under the form of a local formulation, to inhomogeneous and/or optically thin media, including for time-varying situations[25].

According to the hypothesis of this model, the excited electrons and holes form thermal distributions within the emissive material, with parameters that are allowed to vary in space and time[25]. For bulk semiconductors, thermal distributions arise from carrier-carrier and carrier-phonon processes that occur at the sub-ps scale immediately after pulse excitation[26]. In our case, in addition to sub-ps electronic thermalization at the individual NC level, carrier-carrier interactions among neighboring NCs occur via the pronounced FRET effects that characterize our samples. According to previous studies[12], the characteristic time of a single FRET event between two adjacent PbS NCs is much shorter than the carrier lifetimes measured here, providing sufficient time to build up thermal distributions of electrons and holes within the NC film and thus meet the thermalization conditions of Kirchhoff's law. This conclusion is consistent with our previous work on PbS NCs in the steady-state regime, in which we have experimentally demonstrated, using different arguments than those put forward here, that their steady-state emission and absorption properties are also well described by Kirchhoff's law[23,27].

Perhaps the biggest practical difference between the sub-ps carrier thermalization in crystalline semiconductors[26] and the collective thermalization implied by our results is that the total duration of the FRET events exceeds 200 ns, creating an intermediate regime in which the effective bandgap of the NC film is gradually reduced before stabilizing at large wavelengths. The duration of this intermediate regime hinges upon several interdependent factors, such as the width of the inhomogeneous broadening, which sets the spectral interval between the NCs emitting at the shortest and longest wavelengths and also the energetic disorder hampering energy transfers between adjacent NCs. Other factors include the type and length of the ligands capping the NCs, as they influence the nature (i.e. FRET or direct electronic coupling) and rate of the energy transfers. Although a detailed analysis of these factors is outside the scope of this study, it is interesting to look again at the PL measurements performed on a sample cross-linked with much shorter EDT chains (Figure S10), as they are characterized by a faster redshift than that of the other structures examined in this study due to the reduced interparticle distance.

5. Conclusion

In conclusion, we have presented a series of experiments demonstrating that the decay rate of compact layers of PbS NCs is only marginally influenced by their photonic environment, even when the emitters are coupled to resonant optical antennas that dramatically affect their transient PL spectrum and intensity. We have linked this result to the fact that the PL dynamics is not limited to the relaxation at the band edge of the individual emitters. Rather, it involves strong FRET effects among the NCs, unfolding over the course of ~200 ns, that render them largely insensitive to the losses of the photonic environment while simultaneously making them act as an effective semiconductor subject to Kirchhoff’s law. These findings should be of interest for the further development of NC-based optoelectronic devices, especially in terms of carrier lifetime management in solar cells and modulated light sources, as they suggest that the carrier dynamics is predominantly set by energy transfers among the emitters even in the presence of optical resonators. An open question concerns the generality of these results beyond the special case of PbS NCs. In this respect, we note that compact layers of CdSe-CdS/ZnS core-shell NCs were recently shown to obey the local Kirchhoff law in the steady-state[28], raising the prospect that they follow transient dynamics similar to those evidenced here. On the other hand, experiments on HgTe NC assemblies have shown that their PL is quenched when placed in direct contact with metallic structures[29], which is the opposite behavior of the PbS NCs investigated in the present study and elsewhere[18,21–23]. It would also be interesting to extend the study to systems in which FRET among emitters is even more pronounced, such as stacks of CdSe nanoplatlets in which the FRET interaction times reach the ps scale, allowing photocarrier migration over hundreds of nm from their excitation point[30].

ACKNOWLEDGMENTS

We would like to thank Professor Jean-Pierre Hermier for useful discussions about estimating the FRET radius and FRET efficiency. We would also like to thank Corentin Dabard for the absorption measurements of the PbS NCs in solution. We acknowledge support from the European Research Council grant FORWARD (reference: 771688). This work was supported by French state funds managed by the Agence Nationale de la Recherche through the grant Bright (ANR-21-CE24-0012).

REFERENCES

(1) Bharadwaj, P.; Deutsch, B.; Novotny, L. Optical Antennas. *Adv. Opt. Photon.* **2009**, *1* (3), 438. https://doi.org/10.1364/AOP.1.000438.

(2) Baffou, G.; Cichos, F.; Quidant, R. Applications and Challenges of Thermoplasmonics. *Nat. Mater.* **2020**, *19* (9), 946–958. https://doi.org/10.1038/s41563-020-0740-6.

(3) Fukuda, M.; Aihara, T.; Yamaguchi, K.; Ling, Y. Y.; Miyaji, K.; Tohyama, M. Light Detection Enhanced by Surface Plasmon Resonance in Metal Film. *Appl. Phys. Lett.* **2010**, *96* (15), 153107. https://doi.org/10.1063/1.3402771.

(4) Clavero, C. Plasmon-Induced Hot-Electron Generation at Nanoparticle/Metal-Oxide Interfaces for Photovoltaic and Photocatalytic Devices. *Nat. Photon.* **2014**, *8* (2), 95–103. https://doi.org/10.1038/nphoton.2013.238.

(5) Ghenuche, P.; Mivelle, M.; De Torres, J.; Moparthi, S. B.; Rigneault, H.; Van Hulst, N. F.; García-Parajó, M. F.; Wenger, J. Matching Nanoantenna Field Confinement to FRET Distances Enhances Förster Energy Transfer Rates. *Nano Lett.* **2015**, *15* (9), 6193–6201. https://doi.org/10.1021/acs.nanolett.5b02535.

(6) Collison, R.; Pérez-Sánchez, J. B.; Du, M.; Trevino, J.; Yuen-Zhou, J.; O'Brien, S.; Menon, V. M. Purcell Effect of Plasmonic Surface Lattice Resonances and Its Influence on Energy Transfer. *ACS Photon.* **2021**, *8* (8), 2211–2219. https://doi.org/10.1021/acsphotonics.1c00616.

(7) De Torres, J.; Mivelle, M.; Moparthi, S. B.; Rigneault, H.; Van Hulst, N. F.; García-Parajó, M. F.; Margeat, E.; Wenger, J. Plasmonic Nanoantennas Enable Forbidden Förster Dipole–Dipole Energy Transfer and Enhance the FRET Efficiency. *Nano Lett.* **2016**, *16* (10), 6222–6230. https://doi.org/10.1021/acs.nanolett.6b02470.

(8) Blondot, V.; Bogicevic, A.; Coste, A.; Arnold, C.; Buil, S.; Quélin, X.; Pons, T.; Lequeux, N.; Hermier, J.-P. Fluorescence Properties of Self Assembled Colloidal Supraparticles from CdSe/CdS/ZnS Nanocrystals. *New J. Phys.* **2020**, *22* (11), 113026. https://doi.org/10.1088/1367-2630/abc495.

(9) Crooker, S. A.; Hollingsworth, J. A.; Tretiak, S.; Klimov, V. I. Spectrally Resolved Dynamics of Energy Transfer in Quantum-Dot Assemblies: Towards Engineered Energy Flows in Artificial Materials. *Phys. Rev. Lett.* **2002**, *89* (18), 186802. https://doi.org/10.1103/PhysRevLett.89.186802.

(10) Clark, S. W.; Harbold, J. M.; Wise, F. W. Resonant Energy Transfer in PbS Quantum Dots. *The Journal of Physical Chemistry C* **2007**, *111* (20), 7302–7305. https://doi.org/10.1021/jp0713561.

(11) Poulikakos, L. V.; Prins, F.; Tisdale, W. A. Transition from Thermodynamic to Kinetic-Limited Excitonic Energy Migration in Colloidal Quantum Dot Solids. *J. Phys. Chem. C* **2014**, *118* (15), 7894–7900. https://doi.org/10.1021/jp502961v.

(12) Kholmicheva, N.; Moroz, P.; Eckard, H.; Jensen, G.; Zamkov, M. Energy Transfer in Quantum Dot Solids. *ACS Energy Lett.* **2017**, *2* (1), 154–160. https://doi.org/10.1021/acsenergylett.6b00569.

(13) Gao, J.; Johnson, J. C. Charge Trapping in Bright and Dark States of Coupled PbS Quantum Dot Films. *ACS Nano* **2012**, *6* (4), 3292–3303. https://doi.org/10.1021/nn300707d.

(14) Wolber, P. K.; Hudson, B. S. An Analytic Solution to the Förster Energy Transfer Problem in Two Dimensions. *Biophys. J.* **1979**, *28* (2), 197–210. https://doi.org/10.1016/S0006-3495(79)85171-1.

(15) Martins, J. R.; Krivenkov, V.; Bernardo, C. R.; Samokhvalov, P.; Nabiev, I.; Rakovich, Y. P.; Vasilevskiy, M. I. Statistical Analysis of Photoluminescence Decay Kinetics in Quantum Dot Ensembles: Effects of Inorganic Shell Composition and Environment. *J. Phys. Chem. C* **2022**, *126* (48), 20480–20490. https://doi.org/10.1021/acs.jpcc.2c06134.

(16) Moreels, I.; Lambert, K.; Smeets, D.; De Muynck, D.; Nollet, T.; Martins, J. C.; Vanhaecke, F.; Vantomme, A.; Delerue, C.; Allan, G.; Hens, Z. Size-Dependent Optical Properties of Colloidal PbS Quantum Dots. *ACS Nano* **2009**, *3* (10), 3023–3030. https://doi.org/10.1021/nn900863a.

(17) Nguyen, D.-T.; Lombez, L.; Gibelli, F.; Boyer-Richard, S.; Le Corre, A.; Durand, O.; Guillemoles, J.-F. Quantitative Experimental Assessment of Hot Carrier-Enhanced Solar Cells at Room Temperature. *Nat. Energy* **2018**, *3* (3), 236–242. https://doi.org/10.1038/s41560-018-0106-3.

(18) Caillas, A.; Suffit, S.; Filloux, P.; Lhuillier, E.; Degiron, A. Anomalous Absorption in Arrays of Metallic Nanoparticles: A Powerful Tool for Quantum Dot Optoelectronics. *Nano Lett.* **2022**, *22* (5), 2155–2160. https://doi.org/10.1021/acs.nanolett.1c03865.

(19) Carminati, R.; Greffet, J.-J.; Henkel, C.; Vigoureux, J. M. Radiative and Non-Radiative Decay of a Single Molecule Close to a Metallic Nanoparticle. *Opt. Commun.* **2006**, *261* (2), 368–375. https://doi.org/10.1016/j.optcom.2005.12.009.

(20) Rogobete, L.; Kaminski, F.; Agio, M.; Sandoghdar, V. Design of Plasmonic Nanoantennae for Enhancing Spontaneous Emission. *Opt. Lett.* **2007**, *32* (12), 1623. https://doi.org/10.1364/OL.32.001623.

(21) Le-Van, Q.; Le Roux, X.; Aassime, A.; Degiron, A. Electrically Driven Optical Metamaterials. *Nat. Commun.* **2016**, *7*, 12017. https://doi.org/10.1038/ncomms12017.

(22) Wang, H.; Le-Van, Q.; Aassime, A.; Roux, X. L.; Charra, F.; Chauvin, N.; Degiron, A. Electroluminescence of Colloidal Quantum Dots in Electrical Contact with Metallic Nanoparticles. *Adv. Opt. Mater.* **2018**, *6* (2), 1700658. https://doi.org/10.1002/adom.201700658.

(23) Wang, H.; Aassime, A.; Le Roux, X.; Schilder, N. J.; Greffet, J.-J.; Degiron, A. Revisiting the Role of Metallic Antennas to Control Light Emission by Lead Salt Nanocrystal Assemblies. *Phys. Rev. Applied* **2018**, *10* (3), 034042. https://doi.org/10.1103/PhysRevApplied.10.034042.

(24) Würfel, P. The Chemical Potential of Radiation. *J. Phys. C: Solid State Phys.* **1982**, *15* (18), 3967–3985. https://doi.org/10.1088/0022-3719/15/18/012.

(25) Greffet, J.-J.; Bouchon, P.; Brucoli, G.; Marquier, F. Light Emission by Nonequilibrium Bodies: Local Kirchhoff Law. *Phys. Rev. X* **2018**, *8* (2), 021008. https://doi.org/10.1103/PhysRevX.8.021008.

(26) Nozik, A. J. Spectroscopy and Hot Electron Relaxation Dynamics in Semiconductor Quantum Wells and Quantum Dots. *Annu. Rev. Phys. Chem.* **2001**, *52* (1), 193–231. https://doi.org/10.1146/annurev.physchem.52.1.193.

(27) Caillas, A.; Suffit, S.; Filloux, P.; Lhuillier, E.; Degiron, A. Identification of Two Regimes of Carrier Thermalization in PbS Nanocrystal Assemblies. *J. Phys. Chem. Lett.* **2021**, *12* (21), 5123–5131. https://doi.org/10.1021/acs.jpclett.1c01206.

(28) Monin, H.; Loirette-Pelous, A.; De Leo, E.; Rossinelli, A. A.; Prins, F.; Norris, D. J.; Bailly, E.; Hugonin, J.-P.; Vest, B.; Greffet, J.-J. Controlling Light Emission by a Thermalized

Ensemble of Colloidal Quantum Dots with a Metasurface. *Opt. Express* **2023**, *31* (3), 4851. https://doi.org/10.1364/OE.471744.

(29) Bossavit, E.; Dang, T. H.; He, P.; Cavallo, M.; Khalili, A.; Dabard, C.; Zhang, H.; Gacemi, D.; Silly, M. G.; Abadie, C.; Gallas, B.; Pierucci, D.; Todorov, Y.; Sirtori, C.; Diroll, B. T.; Degiron, A.; Lhuillier, E.; Vasanelli, A. Plasmon-Assisted Directional Infrared Photoluminescence of HgTe Nanocrystals. *Adv. Opt. Mater.* **2023**, 2300863. https://doi.org/10.1002/adom.202300863.

(30) Liu, J.; Guillemeney, L.; Abécassis, B.; Coolen, L. Long Range Energy Transfer in Self-Assembled Stacks of Semiconducting Nanoplatelets. *Nano Lett.* **2020**, *20* (5), 3465–3470. https://doi.org/10.1021/acs.nanolett.0c00376.

Observation of quasi-invariant photocarrier lifetimes in PbS nanocrystal assemblies coupled to resonant and non-resonant arrays of optical antennas – Supporting Information

Puyuan He[1], Augustin Caillas[1], Guillaume Boulliard[1], Ismail Hamdi[1], Pascal Filloux[1], Marco Ravaro[1], Emmanuel Lhuillier[2], Aloyse Degiron[1,]*

[1]Université Paris Cité, CNRS, Laboratoire Matériaux et Phénomènes Quantiques, F-75013 Paris, France

[2]Sorbonne Université, CNRS, Institut des NanoSciences de Paris, INSP, F-75005 Paris, France

1. PbS NC synthesis

300 mg of $PbCl_2$ (Alfa Aesar, 99%) along with 100 µL of trioctylphosphine (Alfa Aesar, 90%) and 7.5 mL of oleic acid (OA, Alfa Aesar, 90%) are degassed in a three-neck flask, first at room temperature and then at 110 °C for 30 min. Meanwhile, 30 mg of sulfur powder (S, Alfa Aesar, 99.5%) are mixed with 7.5 mL of OA until full dissolution. This S solution (looking orange clear) is quickly added to the flask under N2 at 80 °C. We stop the reaction after 2 min by adding 1 mL of OA and 9 mL of hexane. The NCs are precipitated with ethanol (VWR, >99.9%) and redispersed in 5 mL of toluene. After repeating this washing step a second time, the pellet is dispersed in 10 mL of toluene (Carlo Erba, >99.8%) with a drop of OA. The solution is then centrifugated as is to remove the unstable phase. The supernatant is precipitated with methanol and redispersed in toluene. The final PbS NC solution in toluene is filtered through a 0.2 µm PTFE filter.

2. Thin film fabrication

The thin films investigated in this study are obtained by spin-coating the PbS NC solution described above on various substrates in a nitrogen glovebox. Unless specified otherwise, their PL properties are investigated under ambient atmosphere, without ligand exchange, after being retrieved from the glovebox. Before starting the measurements, we intentionally let the samples oxidize in air for 12 to 24 hours. During these first hours, the outermost atoms of the NCs are converted into an oxide shell, reducing the volume of PbS and shifting their absorption and PL peaks to smaller wavelengths. After this initial oxidation phase, the NCs are well passivated. Oxidation does not stop, but becomes so slow that the absorption and PL properties do not evolve anymore over the few days required to characterize each sample, allowing reliable and reproducible measurements. The substrates used for the study are glass substrates (Figure 1) and glass substrates patterned with Au metasurfaces (other figures). These metasurfaces and their optical properties are described in detail in the next section of the present document.

3. Full description of the Au metasurfaces and their EIA resonances

The metasurfaces of our study consist of periodic arrays of square Au patches. Their geometrical parameters have been set with finite element simulations, following the design principles outlined in Ref. [1]. For the resonant structures, the geometrical parameters are such that the system does not only sustain dipolar plasmons localized on the Au patches, but also dipolar magnetic resonances occurring between the Au patches. As elaborated in Ref. [1], the interplay between the two types of resonances leads to a sharp optical analog of electromagnetically induced absorption (EIA). For the non-resonant structure that we use as a control sample, we have optimized the geometry so as to minimize its electromagnetic scattering. In practice, rather than simulating the photoluminescence (PL), we take advantage of the reciprocity between absorption and emission and compute the absorption cross-section of a single unit cell using commercial finite element code (Comsol Multiphysics).

The fabrication workflow includes steps of electron beam lithography (using a Raith Pioneer Two system to write the patterns in a bilayer of CSAR 62 and Electra 92 resists from Allresist spun on the substrate), followed by development, deposition of 2 nm of Ti and 25 nm of Au in a Plassys MEB 550S and lift-off. Each metasurface occupies a footprint of 100 µm × 100 µm. Once the fabrication is completed, the metasurfaces are covered by a thin film of PbS NCs (thickness 15 nm – 20 nm). The geometrical parameters and optical properties of the metasurfaces are described and briefly discussed in the next sub-sections.

3.1 Metasurface 1 with a resonance at λ_1 = 1265 nm

Period: 550 nm, size of each square Au patch: 330 nm × 330 nm × 25 nm. As shown with the steady-state PL measurements of Figure S1a and S1b, a sharp PL enhancement is observed at λ_1 = 1265 nm when the structure is covered with a thin film of PbS NCs. The proof that this enhancement is associated with an EIA resonance is given in Figure S1c. This plot represents the dispersion relation of the structure. It features the distinct banana-shaped dispersion of EIA resonances that vanishes when the in-plane momentum k_x approaches zero[1]. On the left side of this panel is plotted the experimental PL dispersion while on the right side is plotted the results of our finite element simulations, revealing an excellent agreement with the measurements. Finally, Figure S1d depicts the norm of the electric field pattern at the EIA resonance in a plane located 15 nm above the top surface of the Au patches.

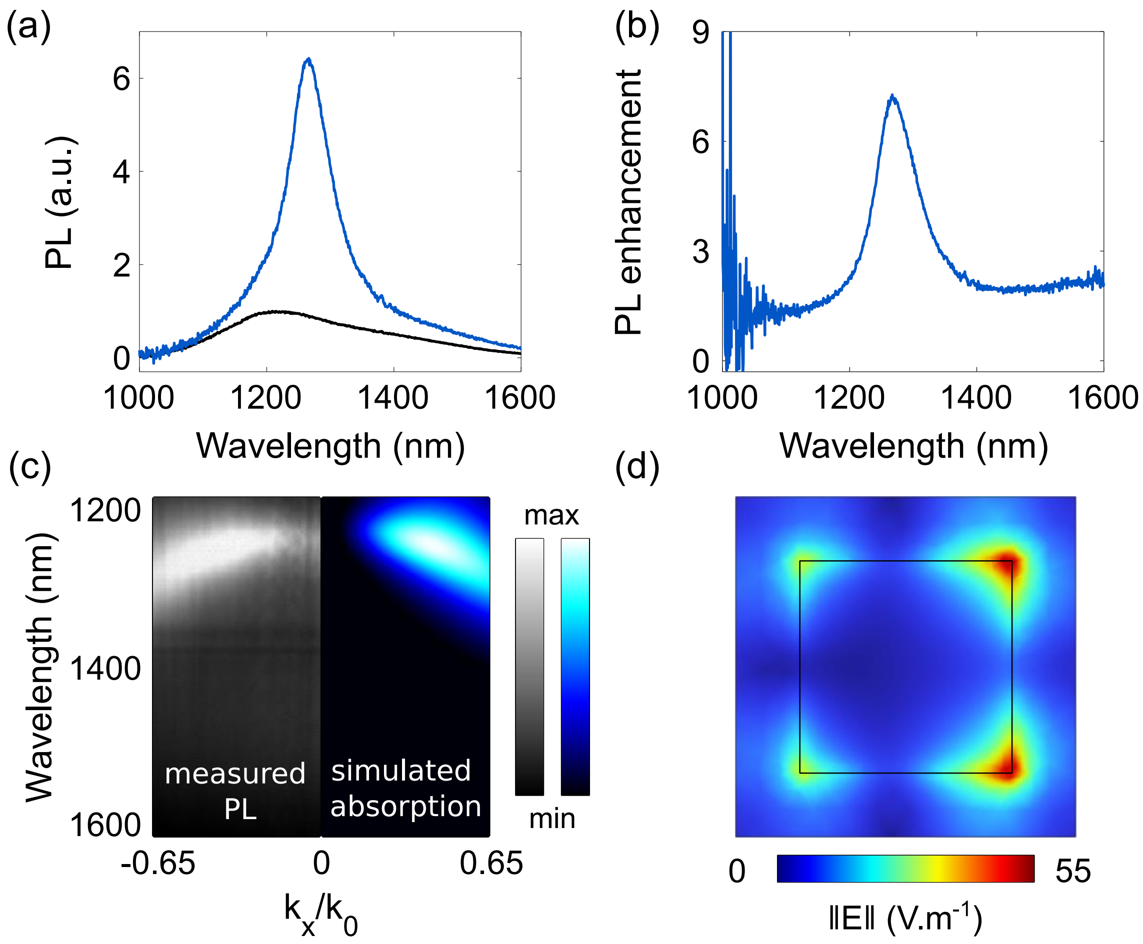

Figure S1. (a) PL spectrum of the sample with a period of 550 nm and 330 nm × 330 nm × 25 nm Au patches (blue curve). Also plotted is the PL spectrum of the PbS NC film on glass (black curve). (b) Ratio between the PL with and without the metasurface. (c) Dispersion relation of the PL recorded above the metasurface (grayscale) vs. simulated TE-polarized absorbance dispersion relation (dark blue to white colormap). (d) Simulated norm of the electric field at the EIA resonance. The field is evaluated in a plane located 15 nm above the top surface of the Au, when the structure is illuminated at oblique incidence with an angle of 20°.

3.2 Metasurface 2 with a resonance at $\lambda_2 = 1480$ nm

Period: 600 nm, size of each square Au patch: 400 nm × 400 nm × 25 nm. The steady-state PL measurements and finite element simulations presented in Figure S2 prove that an EIA resonance is observed and predicted at $\lambda_2 = 1480$ *nm*.

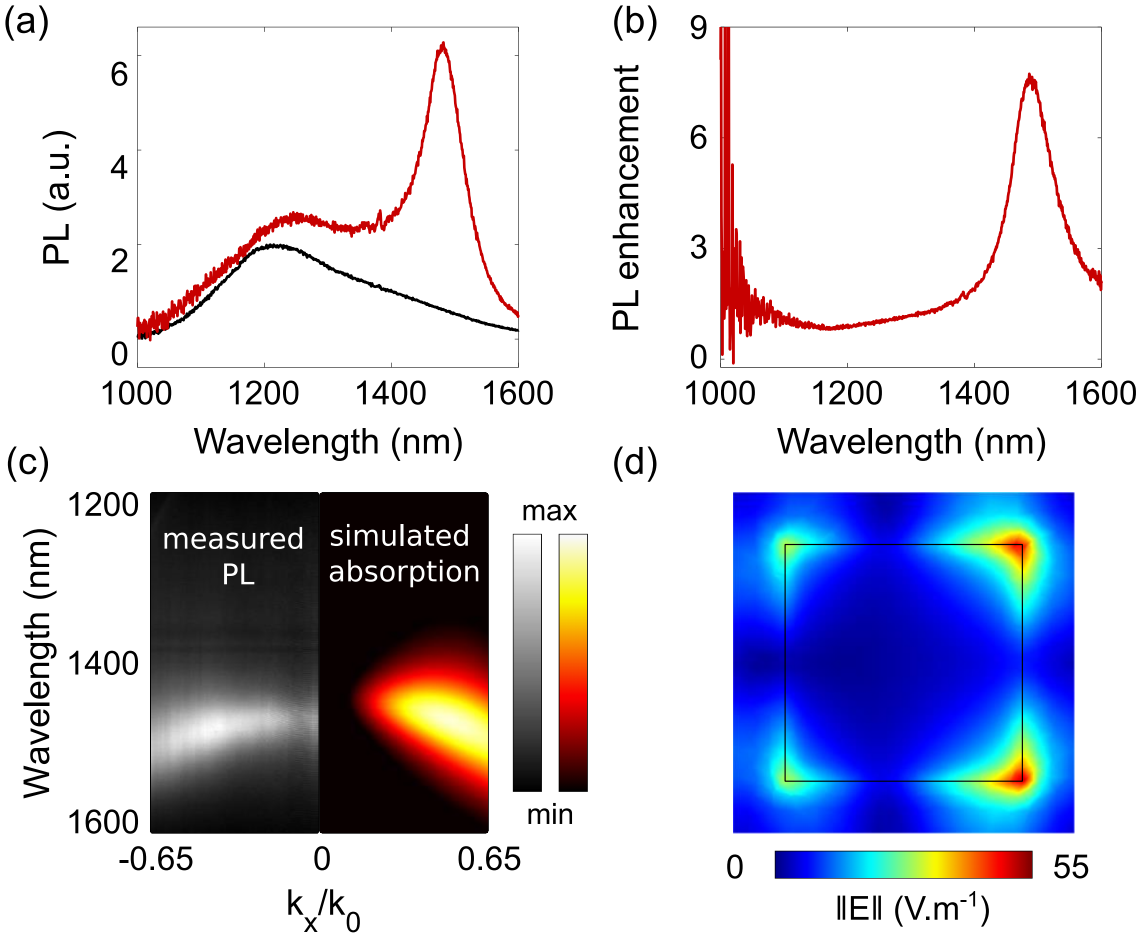

Figure S2. (a) PL spectrum of the sample with a period of 600 nm and 400 nm × 400 nm × 25 nm Au patches (red curve). Also plotted is the PL spectrum of the PbS NC film on glass (black curve). (b) Ratio between the PL with and without the metasurface. (c) Dispersion relation of the PL recorded above the metasurface (grayscale) vs. simulated TE-polarized absorbance dispersion relation (dark red to white colormap). (d) Simulated norm of the electric field at the EIA resonance. The field is evaluated in a plane located 15 nm above the top surface of the Au, when the structure is illuminated at oblique incidence with an angle of 20°.

3.3 Non-resonant metasurface (metasurface 3)

Period: 300 nm, size of each square Au patch: 80 nm × 80 nm × 25 nm. This is a control structure that does not sustain any resonance in the wavelength range under investigation, as confirmed with the steady-state PL measurements presented in Figure S3. Notably, the dispersion relation of Figure S3c is featureless. Notice also how the norm of the electric field computed in Figure S3d is much weaker than in the two previous cases.

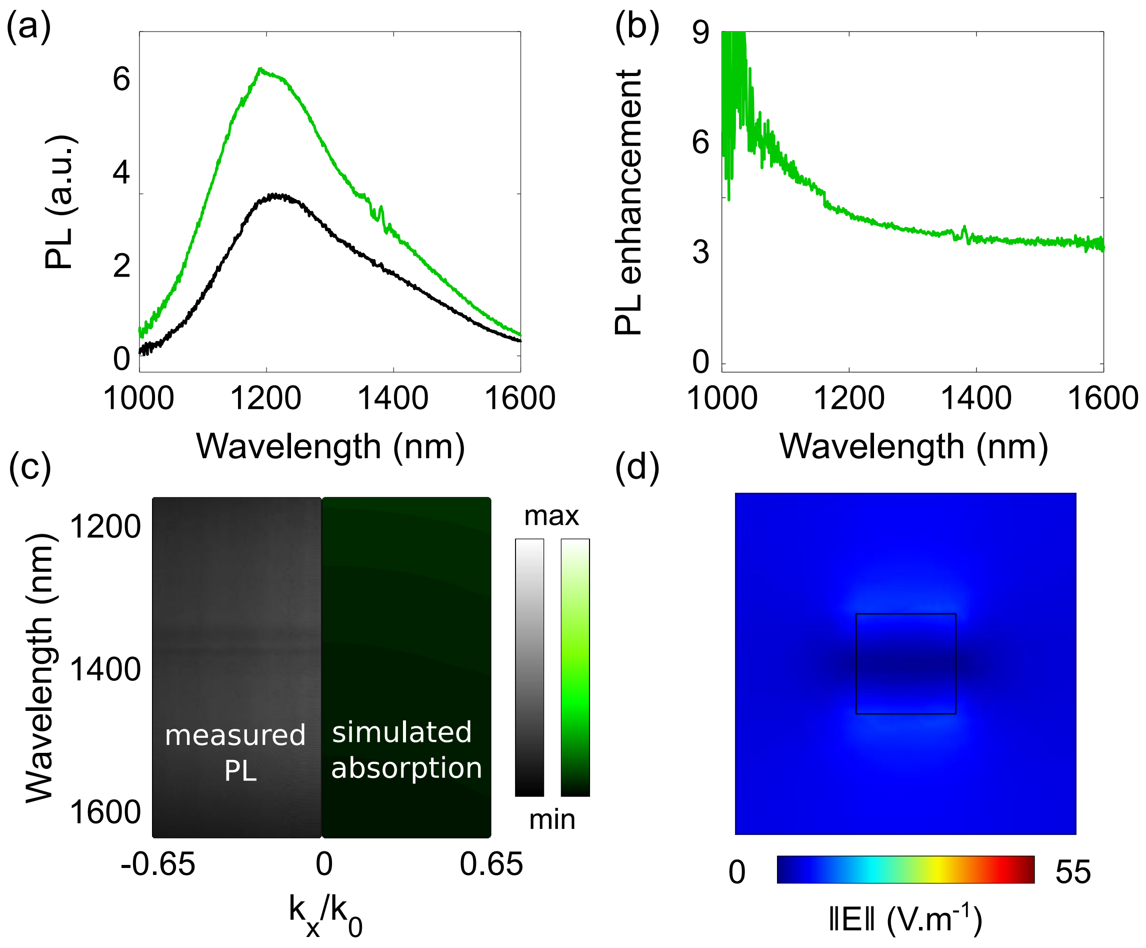

Figure S3. (a) PL spectrum of the sample with a period of 300 nm and 80 nm × 80 nm × 25 nm Au patches (green curve). Also plotted is the PL spectrum of the PbS NC film on glass (black curve). (b) Ratio between the PL with and without the metasurface. (c) Dispersion relation of the PL recorded above the metasurface (grayscale) vs. simulated TE-polarized absorbance dispersion relation (dark green to white colormap). The horizontal dark lines on the experimental data at wavelengths just under 1400 nm are absorption lines of the atmosphere. (d) Simulated norm of the electric field at $\lambda = 1265$ nm (other wavelengths yield essentially the same result for this non-resonant structure). The field is evaluated in a plane located 15 nm above the top surface of the Au, when the structure is illuminated at oblique incidence with an angle of 20°.

4. Experimental setup

4.1 Continuous wave (CW) measurements

The steady-state PL spectra of Figures 1 and 2 have been recorded with a micro-PL setup based on a BX51WI microscope from Olympus equipped with a LCPLN50XIR objective. This objective has a 50 × magnification and a numerical aperture of 0.65. The samples are pumped with a continuous HeNe laser at 633 nm. This laser is filtered with a BG40 colored filter from Thorlabs to eliminate its weak spontaneous emission in the near-infrared. The 50 × objective is used to focus this visible pump onto the sample and to collect the near-infrared PL. The PL signal is subsequently separated from the laser pump using a DMLP950R dichroic mirror followed by an RG780 longpass filter from Thorlabs. Finally, a Telan Lens with a focal length of 200 mm creates an image of the sample in the plane of a 200 µm slit placed at the entrance of an Acton SP2356 imaging spectrograph coupled to a NIRvana InGaAs camera from Princeton Instruments.

To obtain the dispersion relations of Figures S1c, S2c and S3c, an additional Bertrand lens with a focal length of 300 mm is inserted behind the microscope objective to Fourier-transform the PL signal. More details about this setup can be found in Refs. [2,3].

4.2 Transient PL measurements

The experimental apparatus is a time-correlated single photon counting setup featuring an inverted Olympus IX73 microscope equipped with the same 50 × objective as the one used for the CW measurements to focus the picosecond pulses of a LDH-IB-640-B laser diode from PicoQuant (central wavelength 640 nm and repetition rate 1 MHz) onto the sample. The output of this laser is spatially filtered using a single mode fiber (via a 60SMS-1-4-A15-02 laser coupler on one end and a 60FC-4-M20-10 fiber collimator on the other end, both from Schäfter+Kirchhoff) prior injection into the microscope. The near-infrared PL emitted by the PbS NCs is collected with the same objective, separated from the pump using a DMLP950R dichroic mirror and an RG715 colored filter from Thorlabs and finally directed with a multimode optical fiber toward an InGaAs single photon detector ID230 from ID Quantique. The histograms are built using a PicoHarp 300 module from PicoQuant, using the trigger signal from the laser diode driver and the counts sent by the ID230 detector. Because of the long dead time of this detector (20 µs), the PL signal must be attenuated by neutral density filters before entering the optical fiber, in order to avoid pile-ups and other artifacts that would distort the PL dynamics.

All the experiments presented in the main text have been obtained by setting the pulse energy to 250 fJ. The instrument response function, plotted in Figure S4b, has been obtained by replacing the sample with a mirror and by recording the signal originating from the laser itself. Even though the quantum efficiency of our InGaAs detector is almost zero at the laser frequency, enough counts were generated to build a valid histogram using a sufficiently long exposure time (as a control, we have verified that no signal is produced when the laser is turned off).

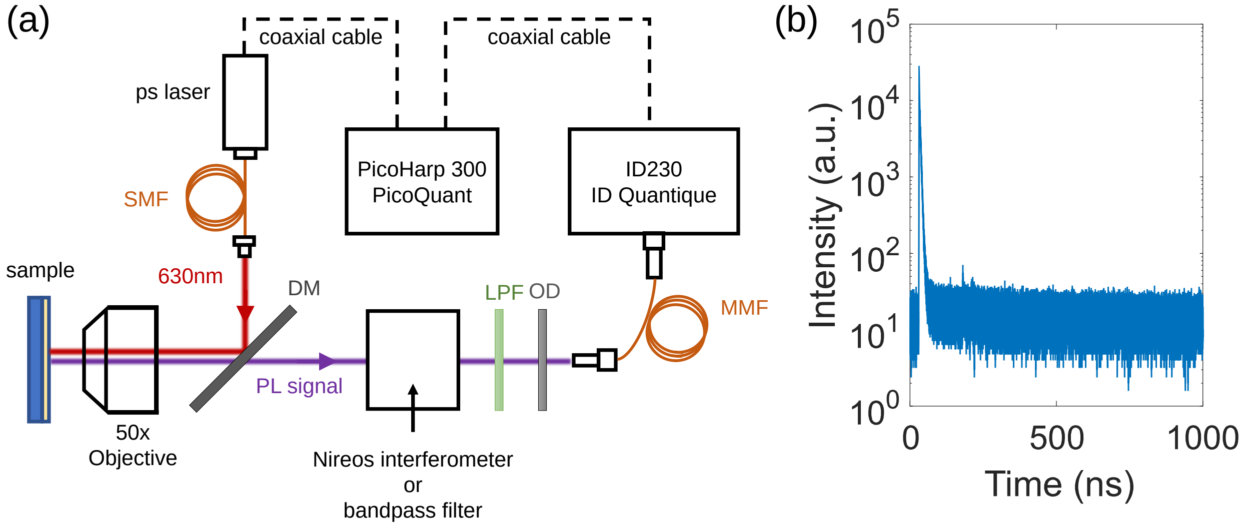

Figure S4. (a) Experimental apparatus. DM stands for DMLP950R dichroic mirror, LPF for RG715 colored filter, OD for neutral density filters, SMF for single mode optical fiber and MMF for multimode optical fiber. (b) Instrument response function of the setup.

Two types of experiments have been performed for this study:

- The transient PL maps displayed in the article and Supporting Information have been recorded by inserting a Gemini wedge interferometer from Nireos before the optical fiber in order to provide a spectral resolution to the measurements. This interferometer works in step-scan mode and produces a time-resolved interferogram that is subsequently Fourier-transformed to obtain the spectral information. The chosen resolution is 20 nm, corresponding to 538 interferometer steps (we have verified that a higher resolution does not change the results) and a binning factor of 64, reducing the time resolution to 256 ps, is applied to smooth out the data. An acquisition time of 30 seconds per interferometer step is necessary to obtain a good signal over noise ratio, leading to approximately 4.5 hours of measurement time for a single PL map. This long exposure time is explained by the fact that the PL signal must be strongly attenuated with neutral density filters to accommodate for the long dead time of the single photon detector as discussed previously.

- The transient PL traces at wavelengths 1200 nm, 1250 nm, 1350 nm, 1450 nm and 1500 nm (Figures 1d, 3c, 3f, 3i, and 4) have been obtained by replacing the Nireos interferometer by bandpass filters with a full width at half maximum of 10 nm (for λ = 1200 nm and 1250 nm) or 12 nm (for the other filters). A binning factor of 16 has been applied to smooth out the data, reducing the resolution to 64 ps. Note that we could have obtained the same results directly from the PL maps recorded with the Nireos interferometer, but we have chosen to use bandpass filters instead in order to improve the signal over noise ratio. The bandpass filter configuration makes it possible to integrate the signal over several minutes, as opposed to 30 seconds per interferometer step for the Nireos configuration (see previous paragraph). Figure S5 illustrates the advantage of this strategy by comparing, for the sample with an EIA resonance at λ_1 = 1265 nm, the PL transients obtained with both methods at five selected wavelengths. It is clear that although both methods yield essentially the same results, the bandpass filter configuration provides much cleaner data.

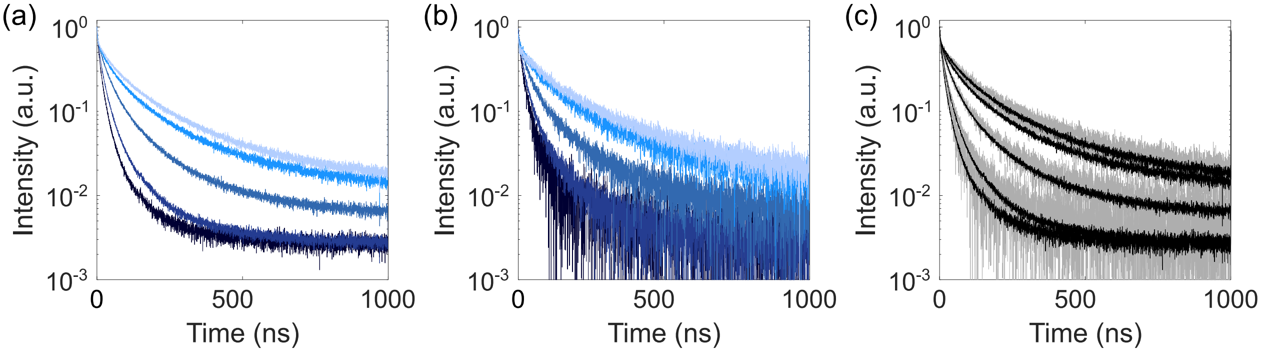

Figure S5. Comparison of the two methods at our disposal to measure PL transients at selected wavelengths. (a) The first method, used in the main text, relies on inserting a bandpass filter centered on the desired wavelength in the optical path. As an illustration, we replot the data of Figure 3c, representing the PL decay of the sample with an EIA resonance at λ_1 = 1265 nm. The wavelengths are the following: λ = 1200 nm, λ = 1250 nm, λ = 1350 nm, λ = 1450 nm, and λ = 1500 nm (from dark to light blue). (b) The second method relies on exploiting the PL maps generated with the Nireos interferometer. The data are much noisier even though we have averaged the data over the same spectral window as that of the bandpass filters used in panel (a). (c) A comparison between the two methods [data of panel (a) in black and data of panel (b) in gray] proves that both methods yield the same results, but with very different signal over noise ratios. Both sets of curves have been smoothen with a time binning factor of 16, corresponding to a 64 ps resolution.

5. Fits of the PL transients

The PL traces of this study have been fitted with Eq. (1). The tables below summarize the fits for all the investigated samples. The accuracy of the fits can be appreciated in Figure S6 where some of them are plotted together with the corresponding experimental curves. The nonlinear short time component τ_0 (see also Figure S7) does not appear at all wavelengths with the low pumping power used in these experiments.

Table S1. Fitting the results of Figure 1d, corresponding to the PL of the film of PbS NCs on glass.

Wavelength (nm)	a_0	a_1	a_2	τ_0 (ns)	τ_1 (ns)	p	τ_2 (ns)
1200	x	592	5	x	38	0.98	450
1250	x	651	14	x	53	0.95	400
1350	x	518	45	x	101	0.88	443
1450	33	171	40	1.6	158	0.52	584
1500	39	119	40	1.4	185	0.35	667

Table S2. Fitting the results of Figure 3c, corresponding to the PL recorded above the metasurface with a resonance at λ_1 = 1265 nm.

Wavelength (nm)	a_0	a_1	a_2	τ_0 (ns)	τ_1 (ns)	p	τ_2 (ns)
1200	x	4044	46	x	25	1.14	250
1250	x	8064	128	x	35	1.15	300
1350	x	3759	158	x	71	1.28	335
1450	193	1168	84	0.8	127	1.21	492
1500	227	896	90	0.9	142	1.03	509

Table S3. Fitting the results of Figure 3f, corresponding to the PL recorded above the metasurface with a resonance at λ_2 = 1480 nm.

Wavelength (nm)	a_0	a_1	a_2	τ_0 (ns)	τ_1 (ns)	p	τ_2 (ns)
1200	x	1581	27	x	25	1.01	200
1250	x	1938	43	x	36	1.05	250
1350	x	2853	114	x	75	1.315	354
1450	540	3215	194	0.7654	122	1.179	490
1500	726	2820	222	0.9882	137	1.066	524

Table S4. Fitting the results of Figure 3i, corresponding to the PL recorded above the non-resonant metasurface.

Wavelength (nm)	a_0	a_1	a_2	τ_0 (ns)	τ_1 (ns)	p	τ_2 (ns)
1200	x	1934	19	x	31	1.02	300
1250	x	2120	27	x	50	1.27	400
1350	x	1580	43	x	128	1.71	553
1450	224	484	47	0.7	169	1.21	580
1500	256	334	41	0.8	211	1.13	679

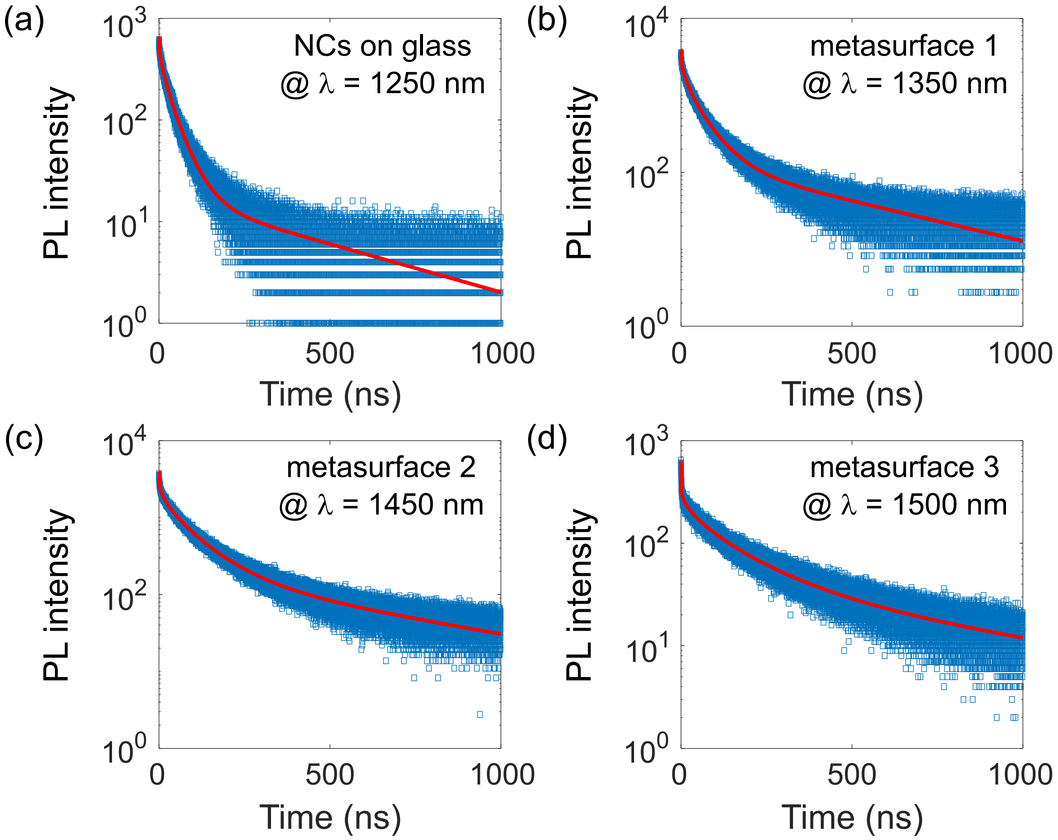

Figure S6. Comparison between a selection of experimental PL transients (blue points) and the results of the fits using Eq. (1) (red curves). Contrarily to the curves plotted in the main text, the experimental transients are not binned by a factor of 16 here (see also section 4.2). Each plot represents a different sample and a different wavelength, as indicated on each panel.

6. Control measurements

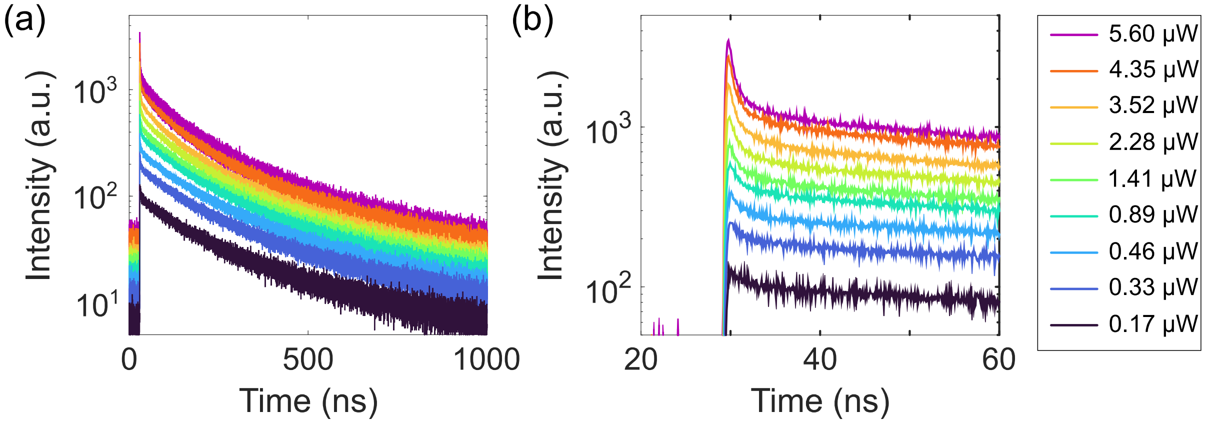

Figure S7. (a) Transient PL traces, recorded at λ = 1450 nm, for the PbS NC film on glass and pump powers indicated on the legend to the right (laser repetition rate: 1 MHz). (b) Close-up of the data at short times.

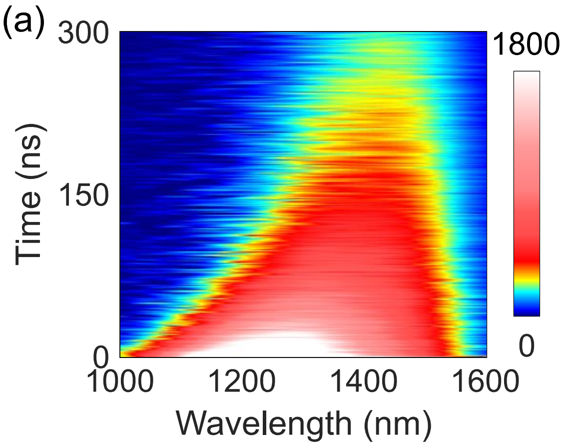

Figure S8. Same experiment as in Figure 1b-c, but with a pump fluence 25 times higher.

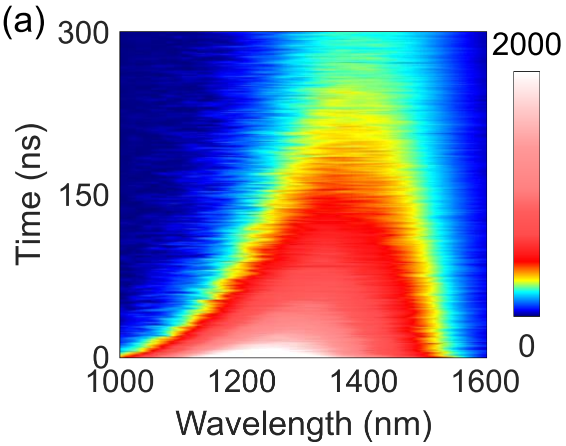

Figure S9. Same experiment as in Figure S8, for a highly-oxidized samples that was left several weeks left in ambient air.

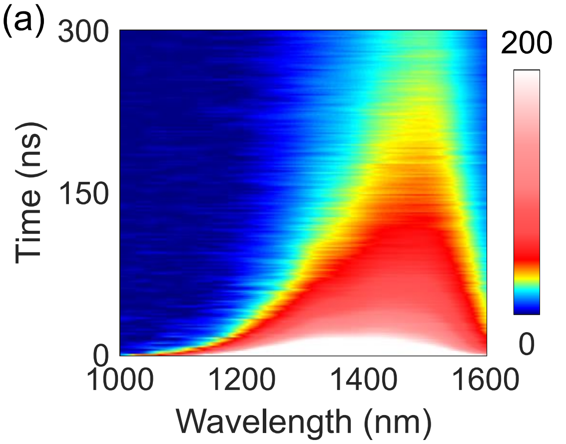

Figure S10. Same experiment as in Figure S8 for a ligand-exchanged sample cross-linked with 1,2-éthanedithiol (EDT). Note that the rate of the FRET-induced redshift is significantly higher than the ~0.8 nm/ns observed in Figures 1, S8 and S9 as a result of the reduced interparticle spacing.

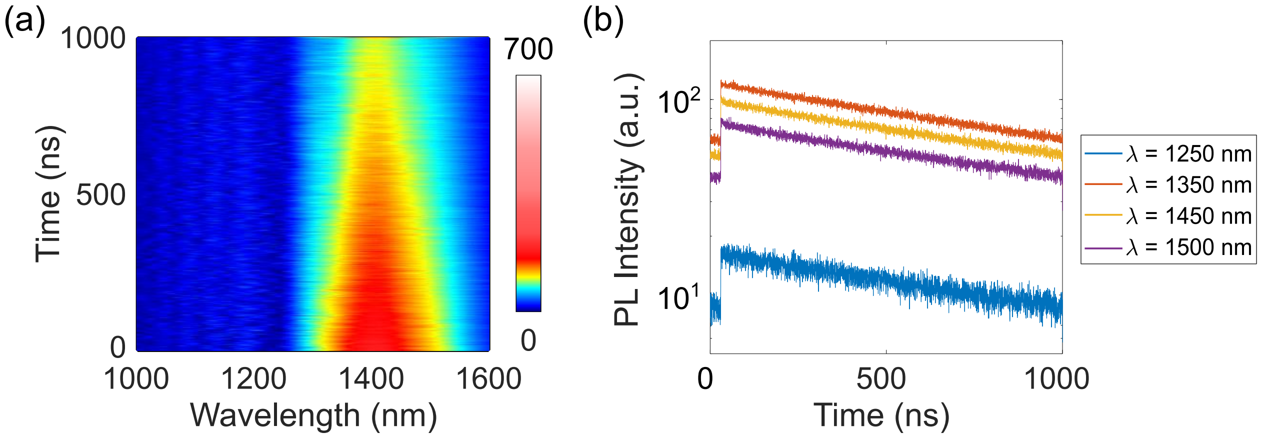

Figure S11. (a) Same experiment as in Figure 1b, except that the PbS NCs are suspended in toluene with a concentration of 4.8 mg/mL rather than forming a compact solid film. Note that in this case, the NCs have a larger radius (i.e. a smaller bandgap) because they are not oxidized contrarily to our thin films measured in ambient air (see discussion about oxidation in section 2 of the present document). (b) Transient PL traces at some representative wavelengths, revealing a mono-exponential decay across the full spectral range.

7. Estimation of the Förster radius and FRET efficiency

We use the textbook model originally developed by Förster that depicts FRET between one dipolar donor and one dipolar acceptor[4,5]:

$$R_0^6(\lambda) = \frac{9\eta\kappa^2c^4}{8\pi N_A n^4}\int \omega^{-4}F_D(\lambda,\omega)\epsilon_A(\omega)\,d\omega,$$

where η is the quantum yield of the donor in the absence of the acceptor, κ accounts for the relative orientation of the dipole moments of the donor and the acceptor (we take $\kappa = 2/3$, corresponding to averaged random dipole orientation), N_A is the Avogadro constant, $n = 1.8$ is the refractive index (taken as an average between the refractive index of PbS and that of the ligands), $F_D(\lambda,\omega)$ is the normalized PL spectrum of a donor emitting at a central wavelength λ in the absence of the acceptor and $\varepsilon_A(\omega)$ is the molar absorption coefficient of the acceptor in the absence of the donor.

The integral is calculated assuming that the PL spectrum F_D of uncoupled PbS NCs emitting at a central wavelength λ is a Gaussian function with a full width at half maximum of 80 nm. Such a large homogeneous linewidth is a representative value for PbS NCs at room temperature[6–9]. The absorption term $\varepsilon_A(\omega)$ has been measured with PbS NCs in solution, at a low concentration of 0.89 mg/mL that ensures that the emitters are sufficiently far apart, and therefore uncoupled, from each other (Figure S12a). Note, however, that this measurement does not strictly reflect the actual properties of the NCs that form the thin films investigated in our study, as the latter have been voluntarily let oxidized in air for 12 to 24 hours to stabilize their properties (see section 2 of the present document). This oxidation step passivates the NCs by converting their outermost layer into a thin oxide shell, reducing the radius of the PbS NCs and blueshifting their absorption.

Figure S12b displays the evolution of R_0 over the spectral bandwidth of our PbS NC films. The calculation of R_0 is largely insensitive to the exact choice of η, n, κ and the full width at half maximum of F_D due to the sixth-power dependence between the two terms of the formula used above. It is, however, sensitive to the actual shape and magnitude of the absorption term $\varepsilon_A(\omega)$. Since we have measured this term with NCs in toluene (Figure S12a), our estimation of R_0 does not take into account the fact that we have systematically let our thin films of PbS NCs oxidize in air to stabilize their properties before proceeding with the measurements.

The actual Förster radius of our samples is most likely larger than the estimation given here because we were able to fit our PL transients with the model given by Eq. (1), which relies on the fact that R_0 is larger than the distance d between neighboring emitters[10]. We have verified that the adjusted parameters of our fits did not change when fitting the experimental data with the more general expression given in Ref. [10] for arbitrary ratios d/R_0. According to scanning electron micrographs of our PbS NC films (Figure S12c), $d \approx 8.5$ nm on average, providing a lower bound for the actual value of R_0.

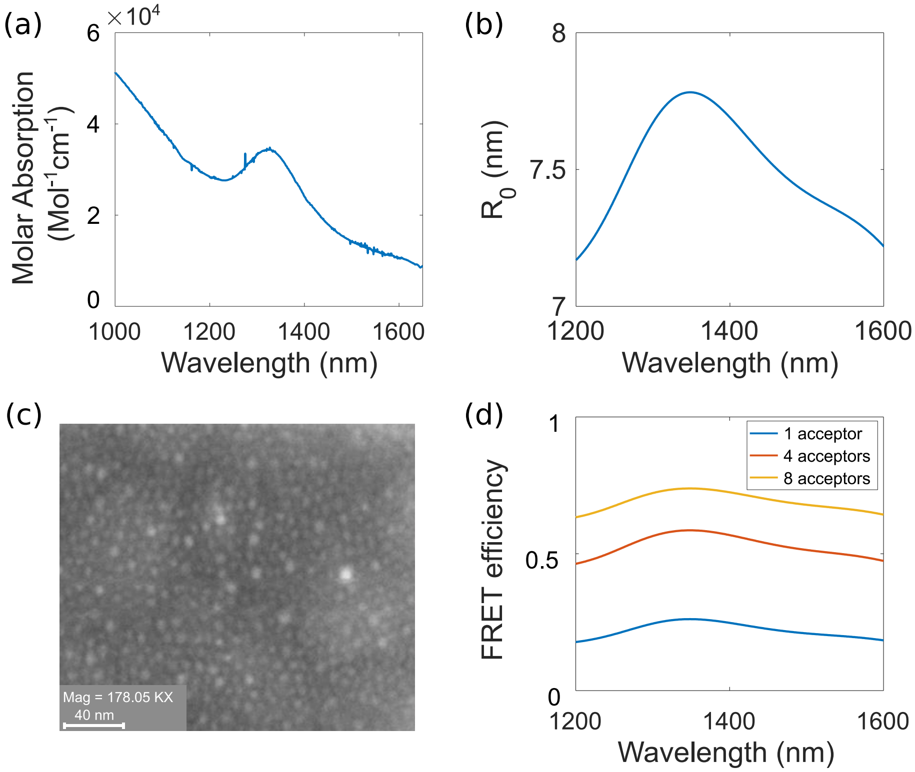

Figure S12. (a) Molar absorption coefficient of the PbS NCs in toluene. (b) Calculated Förster radius R_0 as a function of the wavelength. As explained in the text, this calculation underestimates the actual value of R_0. (c) Scanning electron micrograph of one of our PbS NC films, showing a sizable dispersion in size at the origin of the large FRET-induced redshifts observed in our study. (d) Theoretical FRET efficiency of a single donor for an increasing number of acceptors.

Using the value of R_0 calculated and plotted in Figure S12b, the FRET efficiency between a pair of donor and acceptor is[4,5]:

$$E = \left(1 + \frac{d^6}{R_0^6}\right)^{-1},$$

Given that each NC is surrounded by 6 to 10 neighbors in our films, the overall FRET efficiency is very large, as can be appreciated in Figure S12d where E is plotted for an increasing number of acceptors. This result is another validation that FRET plays such an important role in our experimental results.

Supplementary References

(1) Caillas, A.; Suffit, S.; Filloux, P.; Lhuillier, E.; Degiron, A. Anomalous Absorption in Arrays of Metallic Nanoparticles: A Powerful Tool for Quantum Dot Optoelectronics. *Nano Lett.* **2022**, *22* (5), 2155–2160. https://doi.org/10.1021/acs.nanolett.1c03865.
(2) Schanne, D.; Suffit, S.; Filloux, P.; Lhuillier, E.; Degiron, A. Spontaneous Emission of Vector Vortex Beams. *Phys. Rev. Applied* **2020**, *14* (6), 064077. https://doi.org/10.1103/PhysRevApplied.14.064077.
(3) Schanne, D.; Suffit, S.; Filloux, P.; Lhuillier, E.; Degiron, A. Shaping the Spontaneous Emission of Extended Incoherent Sources into Composite Radial Vector Beams. *Appl. Phys. Lett.* **2021**, *119* (18), 181105. https://doi.org/10.1063/5.0065486.
(4) Novotny, L.; Hecht, B. *Principles of Nano-Optics*; 2006.
(5) Blondot, V.; Bogicevic, A.; Coste, A.; Arnold, C.; Buil, S.; Quélin, X.; Pons, T.; Lequeux, N.; Hermier, J.-P. Fluorescence Properties of Self Assembled Colloidal Supraparticles from CdSe/CdS/ZnS Nanocrystals. *New J. Phys.* **2020**, *22* (11), 113026. https://doi.org/10.1088/1367-2630/abc495.
(6) Peterson, J. J.; Krauss, T. D. Fluorescence Spectroscopy of Single Lead Sulfide Quantum Dots. *Nano Lett.* **2006**, *6* (3), 510–514. https://doi.org/10.1021/nl0525756.
(7) Fernée, M. J.; Jensen, P.; Rubinsztein-Dunlop, H. Origin of the Large Homogeneous Line Widths Obtained from Strongly Quantum Confined PbS Nanocrystals at Room Temperature. *J. Phys. Chem. C* **2007**, *111* (13), 4984–4989. https://doi.org/10.1021/jp067523z.
(8) Caram, J. R.; Bertram, S. N.; Utzat, H.; Hess, W. R.; Carr, J. A.; Bischof, T. S.; Beyler, A. P.; Wilson, M. W. B.; Bawendi, M. G. PbS Nanocrystal Emission Is Governed by Multiple Emissive States. *Nano Lett.* **2016**, *16* (10), 6070–6077. https://doi.org/10.1021/acs.nanolett.6b02147.
(9) Gilmore, R. H.; Lee, E. M. Y.; Weidman, M. C.; Willard, A. P.; Tisdale, W. A. Charge Carrier Hopping Dynamics in Homogeneously Broadened PbS Quantum Dot Solids. *Nano Lett.* **2017**, *17* (2), 893–901. https://doi.org/10.1021/acs.nanolett.6b04201.
(10) Martins, J. R.; Krivenkov, V.; Bernardo, C. R.; Samokhvalov, P.; Nabiev, I.; Rakovich, Y. P.; Vasilevskiy, M. I. Statistical Analysis of Photoluminescence Decay Kinetics in Quantum Dot Ensembles: Effects of Inorganic Shell Composition and Environment. *J. Phys. Chem. C* **2022**, *126* (48), 20480–20490. https://doi.org/10.1021/acs.jpcc.2c06134.